

Validation of Vortical Flow Predictions for a UCAV Wind Tunnel Model.

D. Vallespin, * A. Da Ronch [†] and K.J. Badcock [‡]

University of Liverpool, Liverpool, UK L69 3BX, United Kingdom

O. Boelens [§]

National Aerospace Laboratory, Anthony Fokkerweg 2, 1059 CM Amsterdam, Holland

A study of the aerodynamic behaviour of the Stability And Control Configuration wind tunnel model is presented. Both the sharp and round leading edge versions of the model are analysed in terms of the flow characteristics. A validation of the Reynolds Averaged Navier-Stokes predictions obtained using two block structured codes is made. Both static and dynamic cases are compared with wind tunnel measurements. The vortical flow features are described in detail for the range of conditions analysed. The predictions are in good agreement with the experiments at low angles of attack, whereas for higher incidences, $\alpha > 15^\circ$, discrepancies are seen. A dual vortex structure is present in this region for both leading edge configurations resulting in a highly nonlinear aerodynamic behaviour.

I. Introduction

In recent years there has been interest in understanding the flow behaviour around low sweep delta wings used on some Unmanned Combat Air Vehicles (UCAV). The experimental data obtained from the Stability And Control Configuration (SACCON) UCAV wind tunnel tests^{1,18,19} is used in this paper to validate the capabilities of two RANS codes for predicting vortical flow. The particular applications in mind are the generation of aerodynamic models for flight dynamics and the simulation of manoeuvres featuring aerodynamic history effects.

The current understanding of vortical flow behaviour is summarised in reference⁴ where a distinction is made between slender and nonslender wings, the latter being those with a sweep angle lower than 65° . One of the main differences between the two was shown to be that a dual primary vortex structure occurs over the lower swept wings at high angles of attack. These two vortices are distinct and have the same sense of rotation whereas a single primary vortex structure is present for the slender type.

For a slender, sharp edged delta wing boundary layer separation develops at the leading edge. As a result of this, a free, three-dimensional shear layer emanates from the wing's leading edge which initiates a primary vortex. The regions of high vorticity at the core are surrounded and continuously fed by the shear layer. The shear layer may exhibit instabilities which give rise to vortical substructures and progressively increase the thickness of the primary vortex as it travels downstream. When the primary vortex interacts with the boundary layer on the upper surface of the wing it gives rise to boundary layer separation and the formation of a secondary vortex of the opposite sign of vorticity, as illustrated in Fig. 1. At the centre of the core the axial velocity reaches its maximum value and decreases radially. The vorticity and circulation values are associated with the vortex strength which varies with respect to angle of attack and sweep. Generally, increasing either of these angles produces stronger vortical structures above the wing. Reynolds number is thought to have a noticeable effect on the secondary and tertiary structure formations but not on the

*PhD Student, Department of Engineering

[†]PhD Student, Department of Engineering

[‡]Professor, Department of Engineering, SMAIAA

[§]Research and Development Engineer, Applied Computational Fluid Dynamics, Department of Flight Physics and Loads, Aerospace Vehicles Division.

primary. This is because, for a sharp edged wing at an angle of attack, a separated shear layer will always be produced at the leading edge yielding the primary vortex. The boundary layer is strongly influenced by the magnitude of the Reynolds number. Due to the high rotation of the flow in the vortex core a region of low local static pressure is produced yielding a suction force on the upper surface called non-linear or vortex lift. As a vortex travels axially over the solid, it reaches a point of dramatic flow disruption, termed vortex

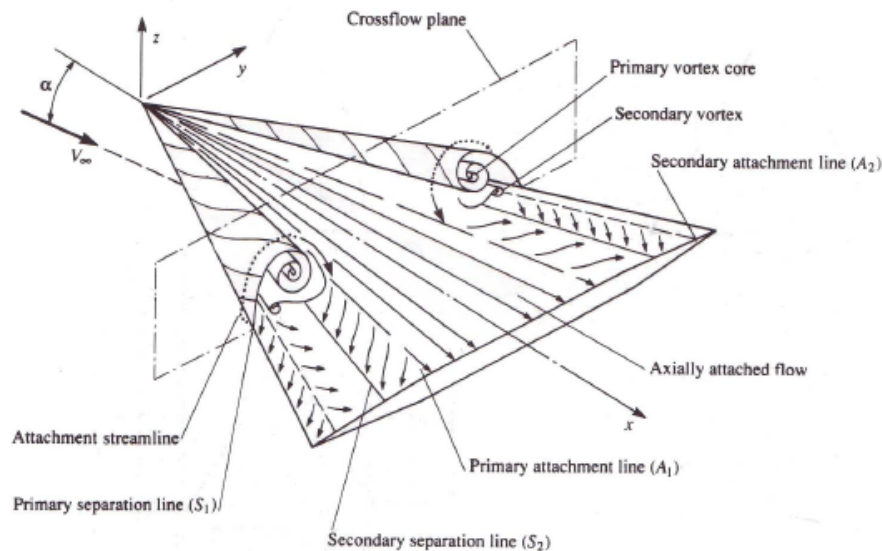
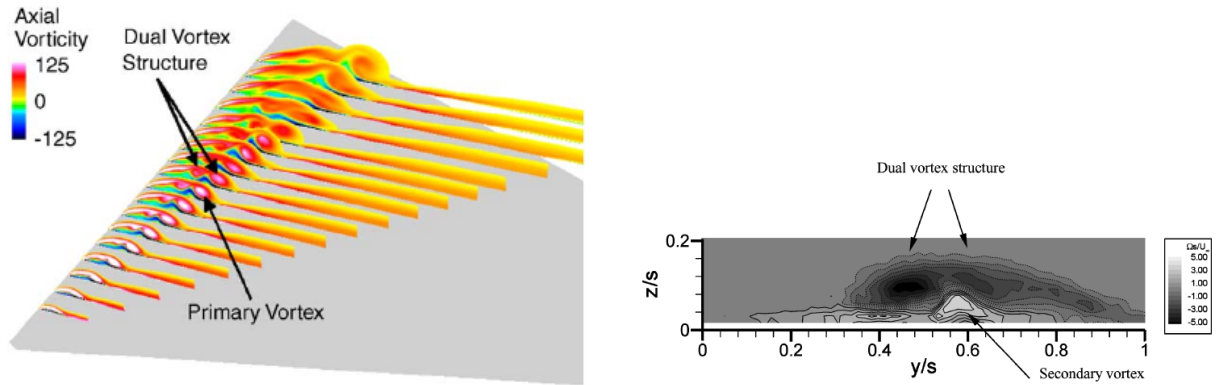


Figure 1. Illustration of the primary and secondary vortices formed over a slender wing.⁵

breakdown, at which the axial flow is known to stagnate. This takes place due to internal and external instabilities and its location travels upstream as the angle of attack is increased. The angle of attack at which breakdown occurs at the trailing edge of the wing is commonly known as the critical angle and when it reaches the apex, the wing is known to be stalled. Gursul⁴ described the post-breakdown region as where the primary vortex core disintegrates into a large number of fine-scale, highly unsteady flow features. Only a large region of vortical flow made up of these small structures can be distinguished. Yaniktepe and Rockwell¹⁴ identified three stages in the low sweep delta wing vortex breakdown process after the region of a well defined filament occurring at the apex. First, small scale undulations, or spiralling, occur at the vortex core associated with the shear layer instabilities and the onset of breakdown. Secondly, the filament is seen to thicken and become small again at what is defined as the pinch off region. Finally, breakdown occurs characterised by an abrupt expansion of the filament where the particles are diffused over a broad area. An increase in pressure accompanies this broken down flow region for which various examples are shown in the present study.

When the sweep angle of a slender delta wing is reduced the flow behaviour around it changes considerably. This has been the topic of more recent studies due to its application for modern UCAV configurations. Taylor and Gursul⁶ concluded from an experimental study with a 50° sweep delta wing at a Reynolds number around 3×10^4 that an elongated region of separated flow transforms into a dual vortex structure. This occurs further downstream from the formation of the primary vortex. Here, as the secondary flow separates from the body surface, it impinges on the separated shear layer emanating from the leading edge splitting it into two vortices of the same sign, as shown in Fig. 2. This gives rise to the second primary vortex which is slightly weaker and smaller than the first vortex. Experiments carried out on a sharp 2% thick delta wing with a sweep of 50° at Reynolds numbers of 10^{46} demonstrated that dual vortical flows may occur at angles of attack as low as $\alpha = 5^\circ$. As the incidence was further increased to $\alpha = 15^\circ$ the clear dual vortex structure disappeared to form a structure that resembles those of highly swept wings, with a primary, secondary and tertiary vortex. Therefore, it can be said that the splitting of the primary vortex into two by the boundary layer vorticity disappears as the angle of attack is increased.

Experiments carried out by Miao et al.¹¹ on a 50° sweep delta wing at a Reynolds number of 7 x



(a) Computed illustration of a dual vortex structure over a 50° delta wing at $\alpha = 5^\circ$.⁴ (b) Crossflow vorticity field at a section across the vortices for a 50° delta wing at $\alpha = 7.5^\circ$.⁶

Figure 2. Illustration of dual vortex structures.

10^3 investigated the role of the leading edge shape in the overall flow behaviour. They looked at the flow over several different types of sharp leading edges, a round and a blunt one and noticed differences in the streamlines and the vortex paths. More specifically, the shapes with bevelling on the windward surface had a leading edge vortex at $\alpha = 10^\circ$ whereas those with blunt shape or bevelling on the leeward surface did not. Fig. 3 shows a schematic of the two types of sharp leading edge shape and the flow around it. Also, the rounded geometry developed a leading edge vortex further downstream than the sharp one, at 20% of the chord. It was concluded that the initial trajectory of the separated shear layer is what determines the overall vortex behaviour above the top surface.

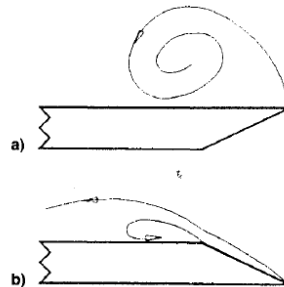


Figure 3. Illustration of the windward (a) and leeward (b) surface bevelling.¹¹

Previous citations in this text referred to studies performed at relatively low Reynolds numbers. Gordnier and Visbal⁷ carried out a study on a 50° sweep delta wing looking at the influence of the Reynolds number on the resulting vortical flow. Their computations and experiments focused on the unsteady behaviour of the flow at three Reynolds numbers: 2×10^5 , 6.2×10^5 and 2×10^6 . They concluded that the vortex breakdown location moved upstream and then downstream again with helical substructures becoming more numerous in the shear layer and developing further upstream as the Reynolds number increased.

II. CFD Formulation

A. Liverpool Solver (Parallel Multiblock)

The parallel multiblock (PMB) solver has been under development over the past 15 years.⁹ The Euler and Reynolds-averaged Navier-Stokes (RANS) equations are discretised on curvilinear, multiblock, body-conforming grids using a cell-centered finite volume method that converts the partial differential equations into a set of ordinary differential equations. The convective terms are discretised using Osher's upwind

method. A monotone upwind scheme for conservation laws variable extrapolation is used to provide second-order accuracy with the Van Albada limiter to prevent spurious oscillations around shock waves. Following Jameson, the spatial residual is modified by adding a second-order discretisation of the real time derivative to obtain a modified steady-state problem for the flow solution at the next real time step which is solved by pseudotime. This pseudotime factor is solved using an unfactored implicit method based on an approximate linearisation of the residual. The linear system is solved in an unfactored form using a Krylov subspace method with block incomplete upper lower preconditioning. The preconditioner is decoupled between blocks to allow a high efficiency on parallel computers with little detriment to the convergence of the linear solver. For the Jacobian matrix of the CFD residual function, approximations are made that reduce the size and improve the conditioning of the linear system without compromising the stability of the time marching.

For the Reynolds numbers needed in this study the turbulence model used is important. Two turbulence models were used to compute the flow around the SACCON model: the $k-\omega$ with a vortex correction¹⁰ and the baseline $k-\omega$ model.¹³ The $k-\omega$ with vortex correction uses the Wilcox two equation formulation with a correction to the amount of turbulence generated inside the vortex core regions, where the flow is thought to be laminar. The baseline $k-\omega$ model utilises the Wilcox model in the inner 50% of the boundary layer and gradually changes to a $k-\epsilon$ towards the boundary layer edge.¹⁰

B. National Aerospace Laboratory Solver (ENSOLV)

The flow solver ENSOLV,¹² which is part of the flow simulation system ENFLOW, is capable of solving the Euler and Navier-Stokes equations on multiblock structured grids for arbitrary configurations. The configuration can be either fixed or moving relative to an inertial reference frame and can be either rigid or flexible. The equations in full conservation form are discretised in space by a second-order accurate, cell-centered, finite volume method, central differences, and matrix artificial diffusion. The artificial diffusion consists of a blending of second- and fourth-order differences with a Jameson-type shock sensor for the basic flow equations and a total variation diminishing (TVD) discontinuity sensor for the turbulence model equations. For steady flow simulations, the discretised time-dependent system of equations is integrated towards the steady-state solution using a five-stage explicit Runge-Kutta scheme. Local time stepping, implicit residual averaging, and multigrid acceleration techniques are applied.

III. Test Case

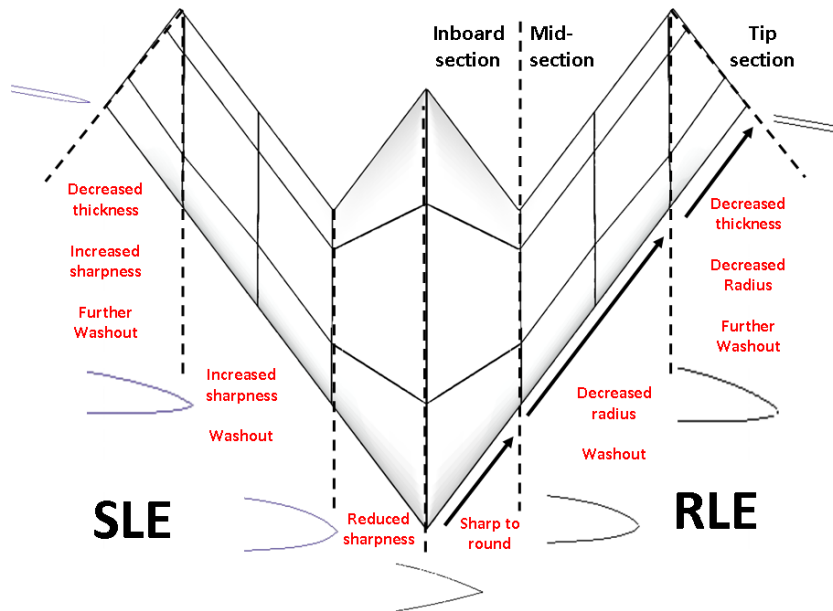


Figure 4. Two different SACCON geometries.

The SACCON UCAV geometry consists of a lambda wing with a sweep angle of 53° and a wing washout of five degrees. Two leading edge geometries were tested during the experimental campaign, one with a partially round leading edge (RLE) and one which is sharp (SLE). A view of the profiles is shown in Fig. 4. There are some important differences in the flow topologies seen experimentally for the two configurations. To illustrate these differences the computed results (described in section 4) at 17° of incidence are shown in Fig. 5. Both sharp and round models exhibit a dual vortex structure at certain angles of attack. The range of angles for which this behaviour happens is larger for the RLE case. The SLE, on the other hand, shows a typical slender wing behaviour after the dual vorticity disappears with increasing incidence. This means that a single primary vortex structure is present over the top surface at high angles of attack. A detailed consideration of the prediction of the RLE model flow field is an important topic of this paper.

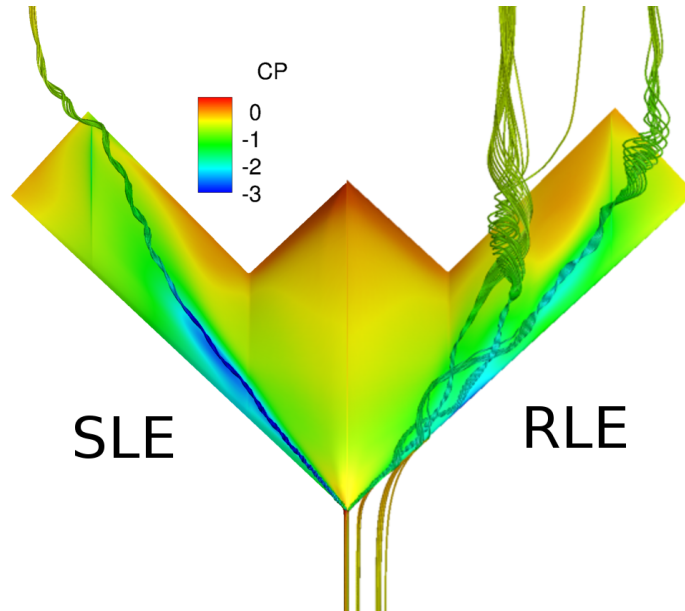


Figure 5. CFD flow solutions for the SACCON UCAV at $\alpha = 17^\circ$ and $Re=1.93\text{mill}$.

The experiments were carried out in the $3.25\text{m} \times 2.8\text{m}$ wind tunnel at DNW Braunschweig.¹ The apparatus used allowed pitching, yawing and plunging motions. The model was mounted on a sting attached to the belly of the model. The moment reference point (MRP) was located at 60% of the root chord. The tests were divided into two parts: static and dynamic.

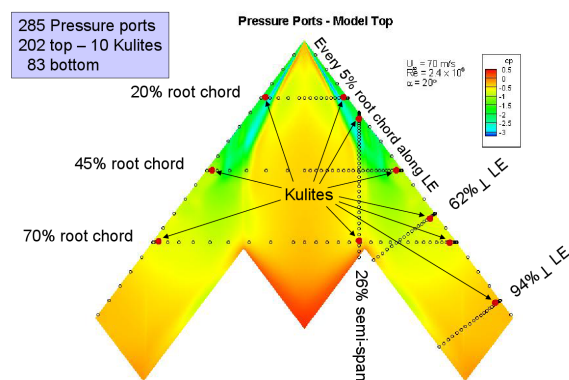


Figure 6. Pressure port and kulite arrangement on the SACCON wind tunnel model.⁸

The static runs consisted of a sweep of the angle of attack, between -15° and 30° , and the sideslip angle, between -15° and 15° . Two runs of each sweep was performed to highlight any repeatability issues.

On the other hand, the dynamic cases consisted of tests in which the model was forced to oscillate with a pitching, yawing or plunging motion. The sting mounting allowed for frequencies of oscillation of 1, 2 or 3Hz. Transition strips were used along the top and bottom parts of the leading edge to trip the flow into a turbulent state.

Pressure taps and kulites were used to obtain pressure data. These were located on longitudinal and transverse sections, as shown in Fig. 6. Particle Image Velocimetry (PIV) measurements were taken over the top surface of the model to gain insight into the flow topology, in particular the behaviour of the vortical structures. The sensors in the belly sting mounting measured the forces and moments of the complete model.



Figure 7. RLE configuration structured grid.

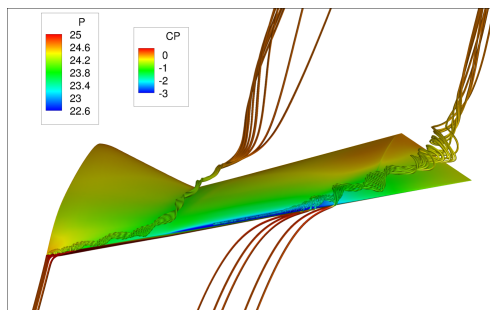
A series of structured multiblock grids were generated using ICEM CFD and inhouse software. First, a 6 million point grid was created for the RLE model from which initial results were obtained and compared with the experiments. A second more refined RLE grid with 7 million points was created as well as a SLE grid with 6 million points. The RLE model grid has a C-blocking around the leading edge and an O-grid at the blunt tip, as shown in Fig. 7 (a) and (b). The SLE, on the other hand, consists of an H-topology around the leading edge and a diamond shaped blocking sitting on the blunt tip. All of these grids were generated without taking into account the sting geometry present in the experiments. The minimum cell spacing normal to the solid geometry is around $0.5 \times 10^{-6}c$ (where c is the reference chord length of the model, $c = 0.479m$) which allows 30 points in the boundary layer at a Reynolds number of 1.93×10^6 . A high cell resolution was purposely used in the region near the model surface in order to capture the vortical behaviour, shown in Fig. 8. Here, the computed flow around the RLE model at an incidence of $\alpha = 15^\circ$ is shown using streamtraces to follow the path of the vortices on the top surface.

IV. Fixed Model Results

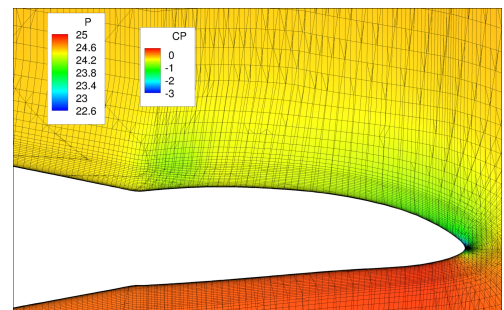
A. Flow structure

The flow around the SACCON UCAV model is dominated by vortical flow effects which show a strong sensitivity to changes in angle of attack and leading edge geometry. The surface pressure coefficient distribution predicted using steady state PMB calculations with the baseline $k-\omega$ model is shown in Fig. 9. The vortical flow development for the SLE configuration for a range of angles of attack, $5^\circ < \alpha < 20^\circ$, can be seen. At low angles of attack, $\alpha < 10^\circ$, the low pressure over the top surface starts to build up but with no clear proof of shear layer separation occurring from the leading edge.

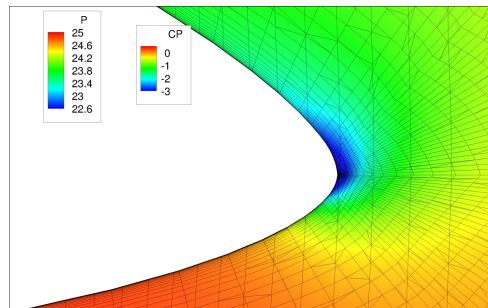
The first clear vortical structure can be seen at an incidence of 10° shown by the stream of low pressure at the wing tip section, also illustrated in Fig. 10 (a) by means of streamtraces. At 13° angle of attack two vortices are present. One starting at the apex and travelling along the leading edge and downstream over the body section at which point it has become very weak, and a second one, the tip vortex, whose onset has travelled upstream close to the wing-body intersection and flows along the leading edge and downstream when it reaches the tip section. Both of these vortices are a result of the shear layer separation at these sections due to the local sharpness of the leading edge. By the time the incidence reaches 15° a single, stronger vortex can be seen originating at the apex. At this stage, the two vortices have merged into one resembling the type of flow topology more common around slender wings. It is clear from the figures that the



(a) Dual vortex structure over the RLE model at $\alpha = 15^\circ$.



(b) Grid resolution at a section along the chord.



(c) Close up of grid resolution through the out-board vortex.

Figure 8. Grid resolution across vortices for the RLE model at 15° incidence.

structure changes rapidly between the angles of 10° and 15° . From this point onwards, the single primary vortex gets stronger as the incidence is increased.

The flow downstream from the apex vortex is seen to expand and become weaker at incidences above 15° . This weakening is clear from the sudden shift from a blue coloured, low pressure, region to a green one further downstream shown in Fig. 9 (d), (e) and (f). The expansion in the vortex core can be seen from the increase in radius of the streamtrace's rotational path shown in Fig. 10 (b). As mentioned in ref.¹⁴ the breakdown of vortices over low swept wings is a gradual one with a relatively elongated breakdown region. As a result of this, the surface pressure coefficient increases along the vortex path. This breakdown region is seen to travel upstream as the angle of attack is increased.

Plotted over the images of Fig. 9 is experimental pressure tap data alongside CFD data plots. The black symbols correspond to the experiments and the red lines to the simulations. In these plots the peaks represent the lowest, negative, values of pressure coefficient. It is clear that the CFD results are in good agreement with the experiments at low angles of attack, below 10° , whereas at higher angles some discrepancies occur. The middle and downstream slices in Fig. 9 (f) show that the location of the vortex in the experiments is different to that of the CFD prediction, the latter showing the vortex further inboard from the leading edge. As the discrepancies are analysed from 15° to 20° incidence, a gradual improvement in the agreement can be seen with the latter plots showing a good agreement. This shows that it is the highly nonlinear region between 13° and 18° angle of attack where the CFD fails to produce an accurate flow prediction.

The disagreement at 15° , 17° and 18° angle of attack coincides with the region in which the merged vortex is being fed by the shear layer emanating from the mid-section of the wing. This is where the blunter leading edge shape is present. Therefore it is reasonable to suspect that the separation point is being predicted further downstream compared with the experiments showed. This could be due to a failure of the turbulence model in predicting separation over blunt leading edges, a grid related issue or a combination of the two. These possibilities are studied in more detail in Section C.

The flow around the SACCON SLE model shows an interesting characteristic which is the existence of two distinct vortices occurring simultaneously over a small range of angles of attack. This is due to the mid section bluntness again, which allows the flow to remain attached over the model's midsection up to high

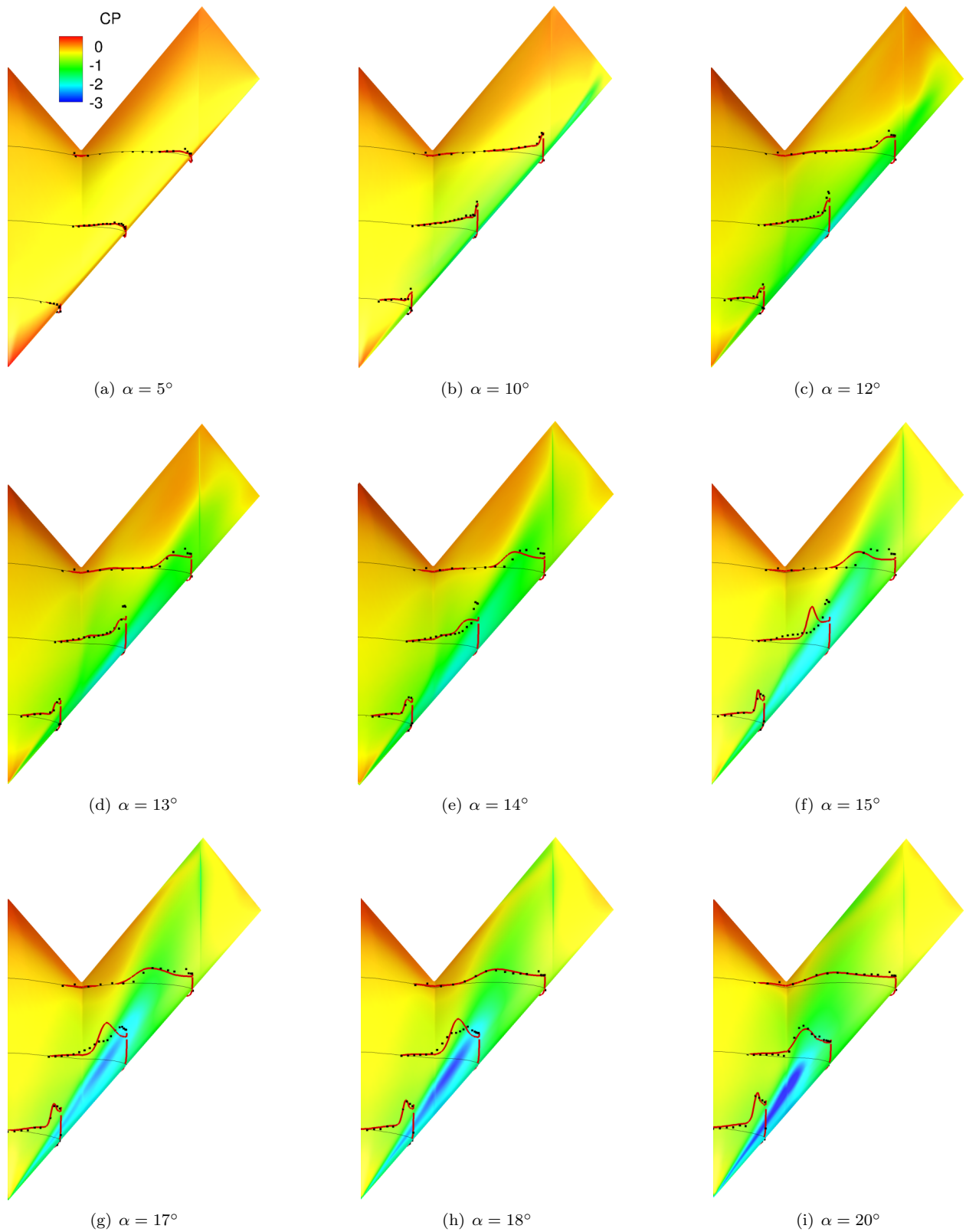


Figure 9. PMB predictions of pressure coefficient distribution (baseline $k-\omega$) with 3D crossplots of experimental measurements for the SLE.

incidences while at the inner and outer sections it separates. This prevents the apex vortex from travelling along the leading edge all the way to the outboard section in one piece up to 15° angle of attack. Hence two distinct vortices occur.

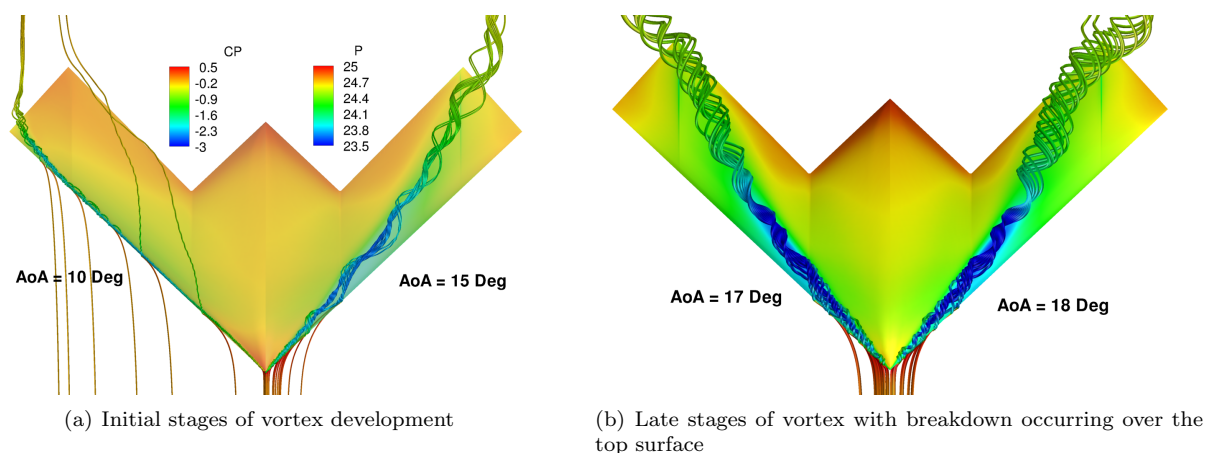


Figure 10. Liverpool's predicted flow topology (baseline $k-\omega$) for the SLE.

The flow behaviour for the SACCON round configuration shows some differences to that seen for the sharp model. The surface pressure distribution for the range of angles of attack from 5° to 19° is shown in Fig. 11. These results were obtained in the same manner as those for the SLE model.

At low angles of attack the flow behaves in a similar way to that of the SLE, with a small outboard vortex seen emanating from the tip section at 10° incidence, shown in Fig. 12 (a). As the incidence increases to 12° , an apex vortex starts to form and a dual vortical structure is present. This type of structure remains up to 19° angle of attack. In this range, the vortices get stronger and the onset of the tip shear layer separation travels inboards. It is at 16° angle of attack that the tip vortex is seen to jump as it travels inboard. From here to around 19° incidence a slow merging of the two vortices occurs.

The dual vortical flow topology becomes clearer from the streamtraces shown in Fig. 12 (a) at 15° angle of attack. In Fig. 12 (b) at 17° incidence, an image during the vortex merging process can be seen. Vortex breakdown is present at 17° and 18° of incidence where the streamtraces change in colour as the spiral increases in size.

In order to look at the flow separation behaviour in more detail, slices across the flow solution were taken and the axial velocity values were compared against PIV measurements carried out by DLR during the experimental campaign at Braunschweig, see Ref.¹⁹ Angles of attack of 16° and 18° are shown in Figs. 13 and 14, respectively, since it is for these cases that comparisons disagree the most. At 16° of incidence the PMB results show two flat vortices which have already started to merge into one and a third one present in the aft slices originating at the trailing edge. The vortex core axial velocity is seen to decrease as it travels downstream but no reversed flow is present therefore no vortex breakdown can be said to occur. The PIV results show a slightly different story with attached flow around the leading edge at sections 0.45c and 0.51c and a group of small vortices further inboard. In the aft sections, from 0.61c to 0.85c, the flow is seen to separate from the leading edge forming a vortex which increases in size as it travels downstream. The small vortices further inboard are seen to merge into a larger structure, thus, having two distinct vortices present with a region of reattached flow between them. This reattachment is not seen in the CFD predictions. The PIV data also shows a pocket of reversed flow at the aft sections near the leading edge, suggesting another vortex core is present and it is broken down. The inboard vortices seen in the experiments at the forward sections are not originating at the leading edge but over the model's surface. This suggests that the cause of the formation of these weaker vortices is the adverse pressure gradient due to the thickness of the wing, which the CFD model does not capture correctly. Looking at the flow at 18° incidence in Fig. 14, section 0.45c has attached flow around the leading edge according to the PIV data. At section 0.51c the PIV data shows a clear three vortex structure which then merges into two vortices further downstream, before breaking down. This breakdown behaviour can be seen by the reversed flow present at the core of the vortex from section 0.70c onwards. The PMB results show a more smeared solution, with the two vortices remaining flat above

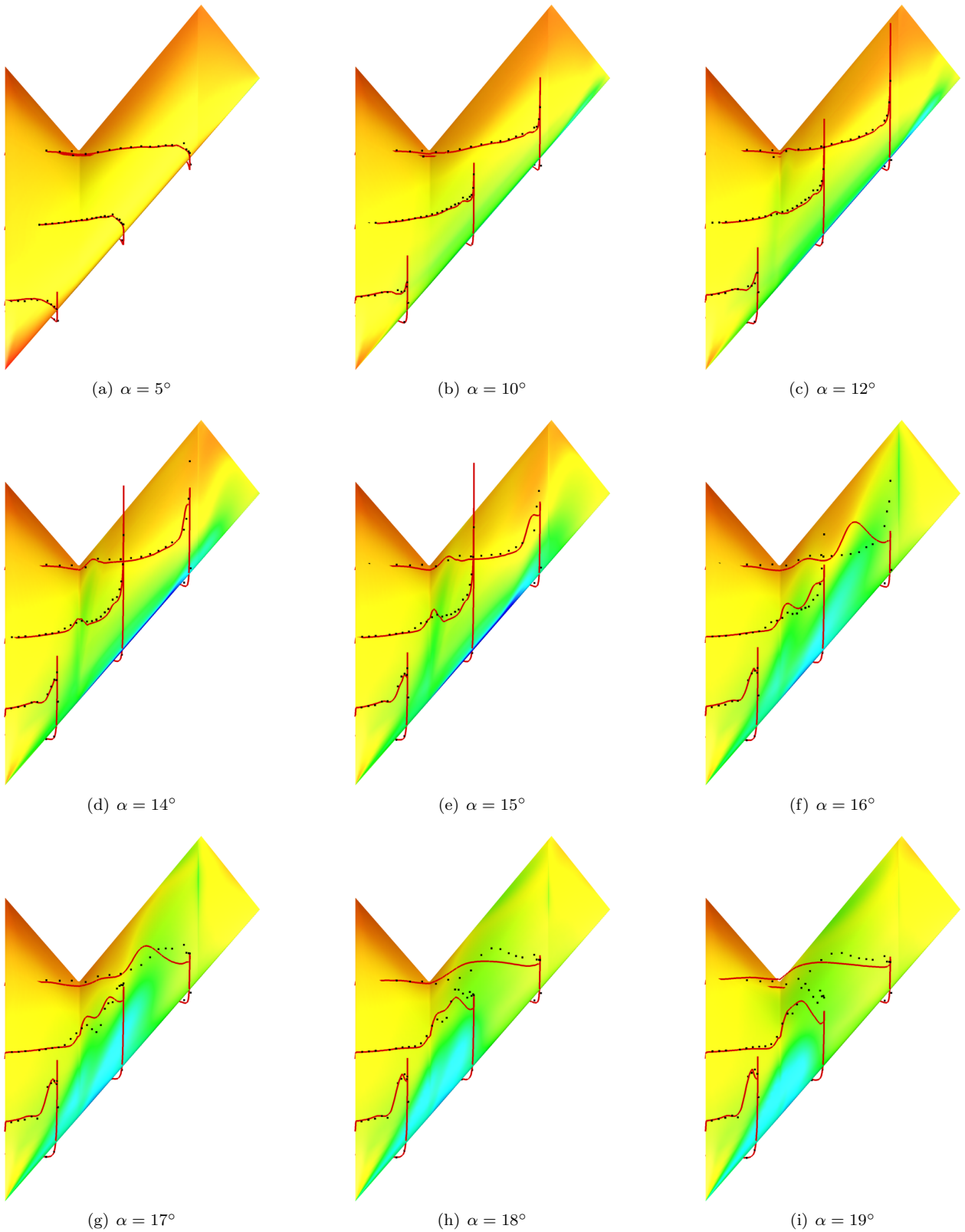


Figure 11. PMB predictions of pressure coefficient distribution (baseline $k-\omega$) with 3D crossplots of experimental measurements for the RLE.

the surface and merging into one structure by the time they reach section 0.64c. By this point, the axial flow velocity at the core has reversed, meaning there is an offset in breakdown position of around 0.06-0.19c with respect to the PIV.

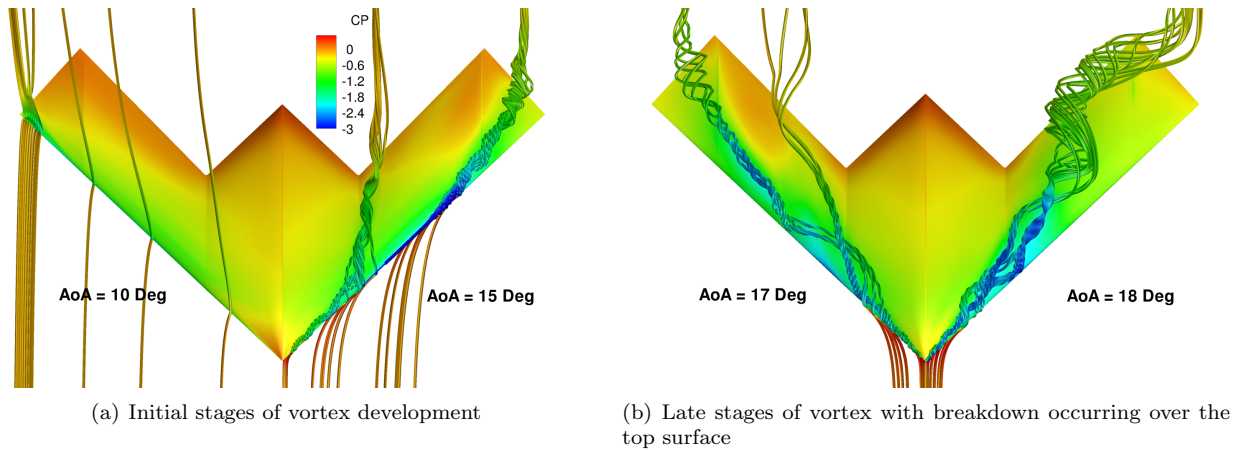


Figure 12. Liverpool's predicted flow topology (Baseline $k-\omega$) for the RLE.

Similar problems are evident in the validation of the CFD using the SLE and RLE cases. In the case of the RLE flow, the noticeable disagreements start to occur at 16° incidence, in both vortex strength and location. Not surprisingly, this is where the tip vortex jumps inboard and it is this same effect that starts to cause the disagreement in the SLE validation, at around 14° . Overall, the main difference is that the flow over the RLE model has a dual vortex structure for a wider range of angles of attack, from 12° to 18° . This is a consequence of the slow merging of the two primary vortices. The PIV data shows the flow separation behaviour around the blunt leading edge section and the inadequate predictions produced from the $k-\omega$ turbulence model. Also, by inspecting the pressure coefficient crossplots, the vortices being predicted seem to be slightly weaker compared with those measured in the experiments for both geometries.

B. Integral data

This section evaluates the force and moment predictions. Where possible, an attempt is made to explain the non-linear characteristics of this data based on the flow behaviour shown in the previous section. The crossplots of lift, drag and moment coefficients are shown in Figs. 15 and 16.

Fig. 15 (a) shows the lift coefficient values as a function of angle of attack for the SACCON SLE obtained from the experiments and a range of steady state simulations. The plots follow a linear trend up to an angle of attack of 13° where they start to follow a shallower path after an initial steepness. Beyond 20° incidence the plots become relatively flat due to a progressive wing stall. This occurs as the vortex breakdown position travels upstream towards the apex. Due to this, the vortex induced suction force becomes less predominant which causes this deficit in lift. It can also be seen that the agreement between the two sets of data is good in the linear and non-linear regions with a slight offset throughout. This offset is likely to be due to the effect of the belly sting mounting present in the experiments and not modelled in the CFD calculations.

The drag predictions from the PMB calculations also show a good agreement with the experimental data, although with an increasing offset as the angle of attack is increased, see Fig. 15 (b).

The pitching moment behaviour is the most interesting of the three since it shows a highly nonlinear behaviour, Fig. 15 (c). The simulations predict the main characteristic drawn from the experiments which is the drop and rise in pitching moment during the tip vortex displacement. The plots increase linearly up to 12.5° at which point the values start to decrease into a dip with its lowest point at around 15° . As the incidence is further increased, the moment recovers reaching a new maximum at an angle of attack of 22° .

The first clear signs of vortex formation in the predicted results appear at 10° of incidence at the tip section. This vortex is the first to emerge and start to travel towards the apex. At 12° of incidence the apex vortex starts to form. But it is when the tip vortex, as it travels inboard, jumps along the middle section of the wing and starts to merge with the apex vortex, at 13° angle of attack, that there is a sudden dip in the

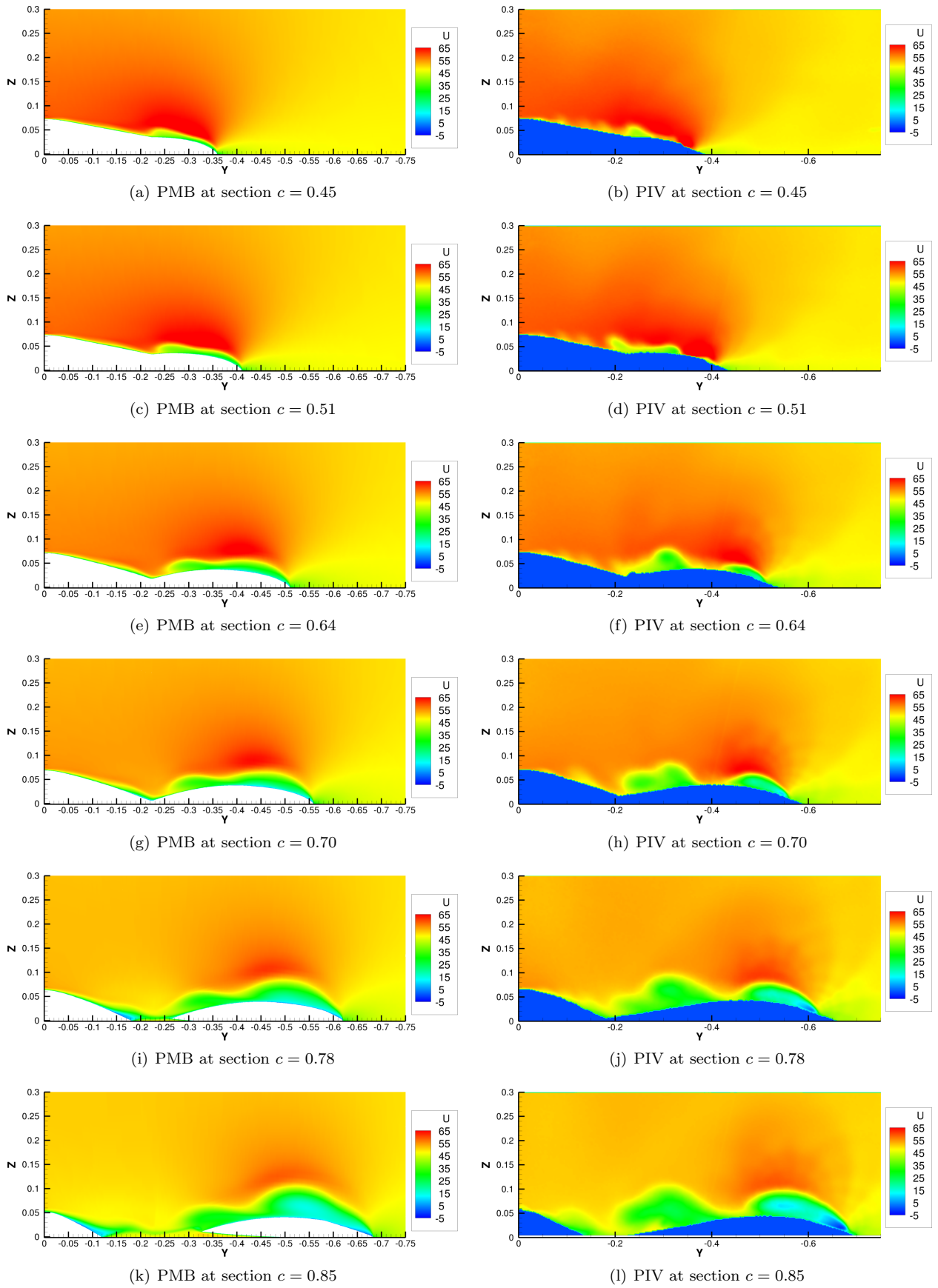


Figure 13. PMB data comparison with PIV measurements for the RLE model at $\alpha = 16^\circ$.

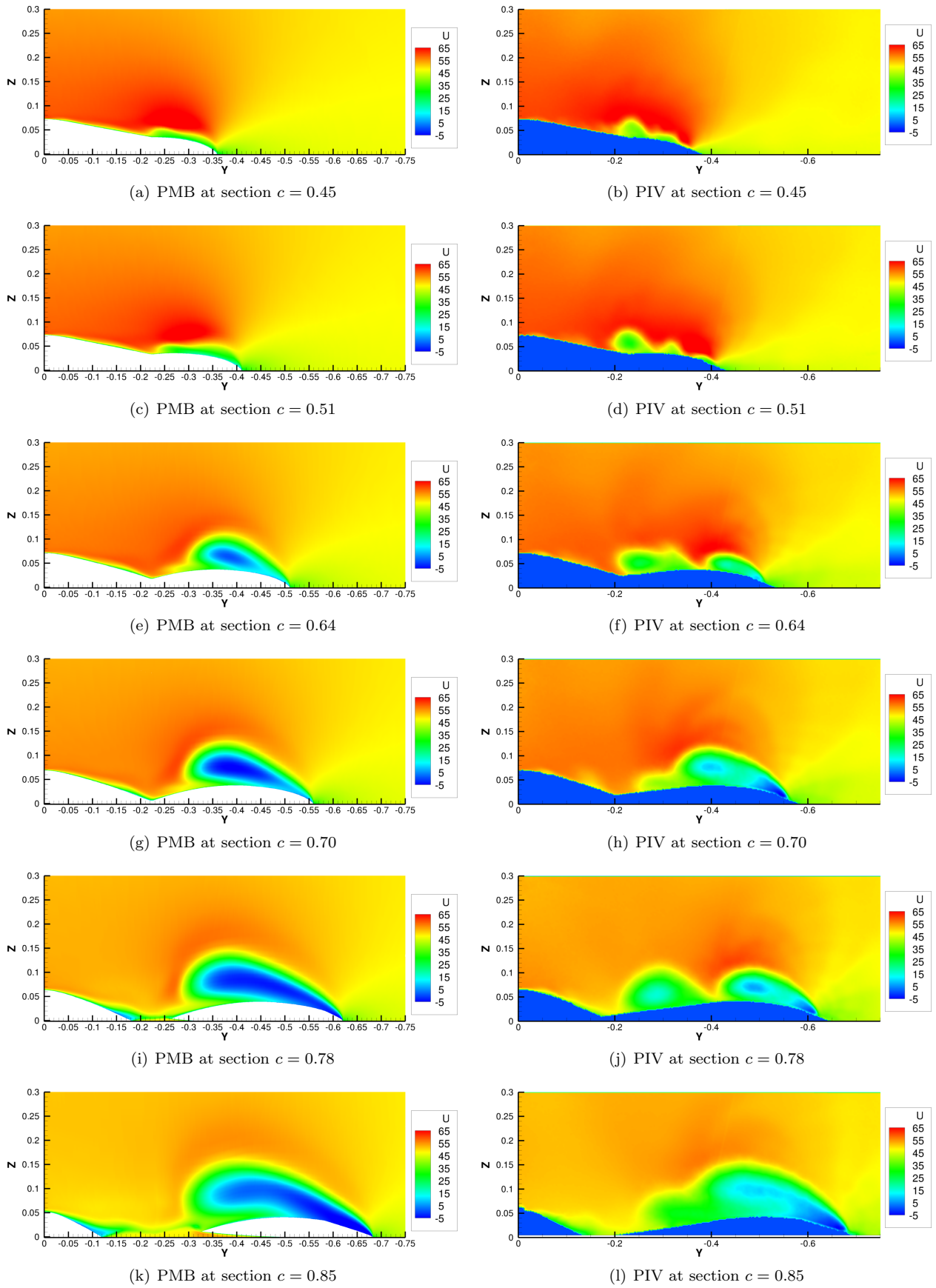
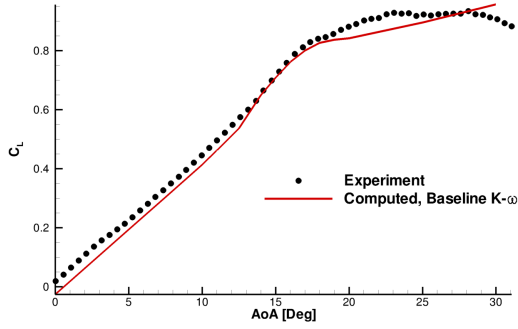
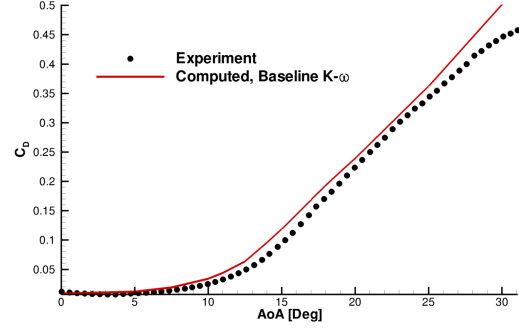


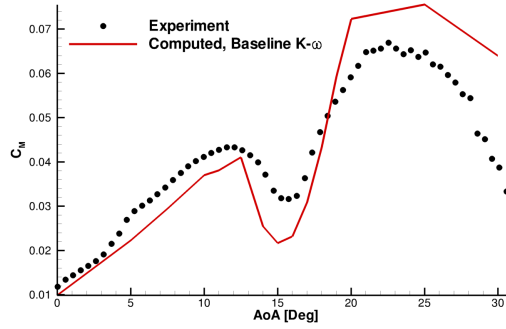
Figure 14. PMB data comparison with PIV measurements for the RLE model at $\alpha = 18^\circ$.



(a) C_L against angle of attack.



(b) C_D against angle of attack.



(c) C_M against angle of attack.

Figure 15. Integral data from experimental results and PMB computations for the sharp model.

moment plot. This is caused by the resulting strong suction in the aft upper surface region. Then, as the apex vortex becomes stronger, due to the increasing incidence, a large region of high vortex suction occurs at the forward section. For this reason and the fact that the vortex breakdown position moves gradually upstream, the pitching moment coefficient plot recovers again to a new maximum value.

The SLE and RLE integral results show noticeable differences, as would be expected from the flow topologies seen in the previous section. Fig. 16 (a) shows the experiment and predicted lift curves. The linear slopes of the two curves are in good agreement although there is an offset between the two due to the effect of the sting mounting, as seen from other SACCON CFD studies.^{15–17} The drag coefficient results, Fig. 16 (b), show a slight offset between the predictions and the experiments for the RLE, similar to that present for the SLE results.

The pitching moment plot for the RLE has some similarities with that of the SLE although generally the behaviour has more abrupt changes. In order to locate the regions of the flow around the body affecting the pitching moment plot, Fig. 17 shows the difference in moment contribution over the surface area between two solutions at different incidences of the RLE model. The blue regions show a positive moment contribution (pitch up), and the red represents a negative one (pitch down). The experiments show an initial linear part up to an incidence of 10°. In Fig. 17 (a) and (b) a positive increase in Δ Moment in the region near the apex can be seen. The negative influence of the outboard, aft section is not large enough to counteract the pitch up moment in this range of angles of attack. As the tip vortex starts to gain strength over the tip section from 10° onwards, the pitching moment plots are seen to flatten. Fig. 17 (c) shows clearly the increase in pitch down effect from the tip section as the incidence is increased from 10° to 14°. At the same time, the contribution from the apex region has decreased slightly compared to the lower incidences, hence the change in behaviour on the plot. Fig. 17 (d) shows a pitch up (red) area in the tip section due to the inboard displacement of the vortex between 14° and 15° incidence. This causes the small spike in pitching moment coefficient before the large drop at 16°. Up to this point the baseline $k-\omega$ predictions are in good

agreement with the experiments with an offset throughout. The drop at 16° is similar to that seen for the SLE and caused by the sudden jump of the outboard vortex as it travels inboards merging with the apex vortex. The same vortex behaviour causes this drop on the RLE wing, as shown in Fig. 17 (e). The large blue region in the aft part of the middle section of the geometry illustrates how the suction effect from the vortex causes the pitch down moment. The computed results from the baseline $k-\omega$ model predict a more pronounced drop than the experiments, which is due to the overprediction of vortical strength as mentioned in the previous section. Figs. 17 (f), (g), (h) and (i) show that the reason for the steep increase in moments from 16° to 20° is the strong vortex suction over a small elongated region near the apex. The region beyond 18° angle of attack is characterised by a separated unsteady flow over most of the top surface of the wing.

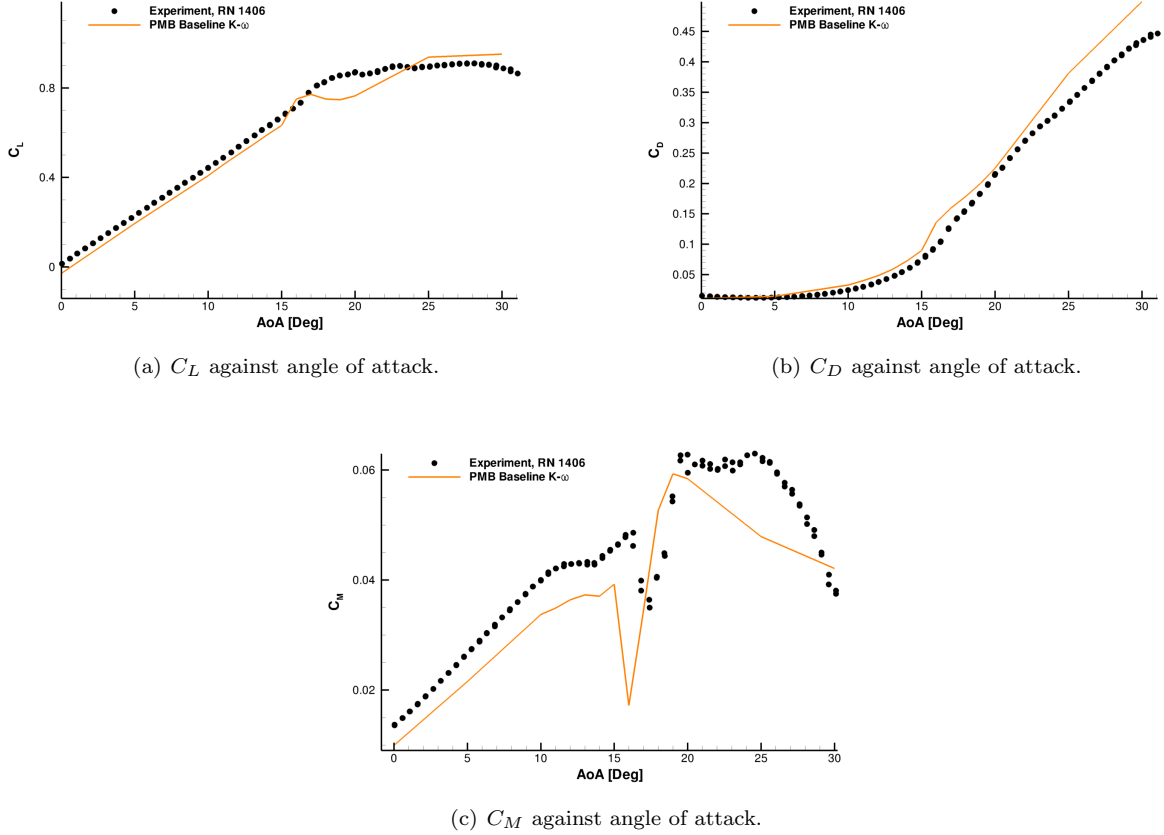


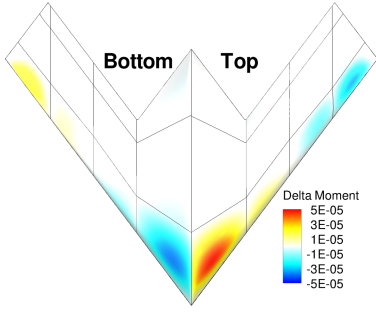
Figure 16. Integral data from experimental results and PMB computations for the round model.

From this validation, it is reasonable to say that the CFD and experimental results are in better agreement for the SLE model than for the RLE. This is due to the added complexity of the flow around the RLE configuration with a dual vortex structure over a wider range of angles of incidence.

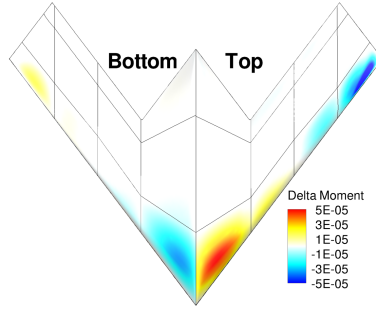
C. Evaluation of Simulation Options

This section presents a study of the different simulations that were carried out for the analysis of the flow around the SACCON configuration. A grid refinement study was done to assess the grid size required to achieve grid convergence. To this end a family of structured multi-block grids was generated using the grid generation tools available in NLRs flow simulation system ENFLOW.¹² These grids all have the same topology consisting of 51 blocks. Each grid incorporates three multi-grid levels. The first cell spacing normal to the solid surface was around $1 \times 10^{-5}c$ on the coarsest multi-grid level, ensuring a y^+ value of approximately one on this grid level. More details on the grids can be found in Table 1.

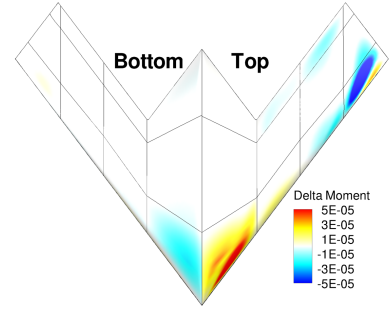
Steady-state simulations were performed for $\alpha = 10^\circ$, $M=0.17$ and $Re=1.93$ million using NLRs flow solver ENSOLV. The TNT $k-\omega$ turbulence model was used in fully turbulent mode. On each grid level 1500



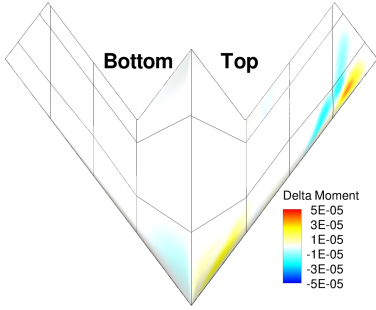
(a) Difference between $\alpha = 0^\circ$ and 5°



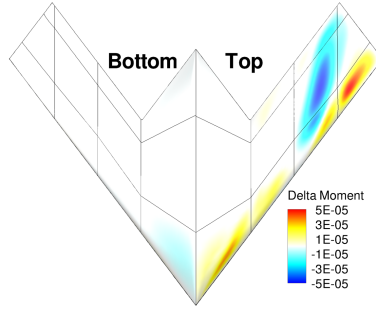
(b) Difference between $\alpha = 5^\circ$ and 10°



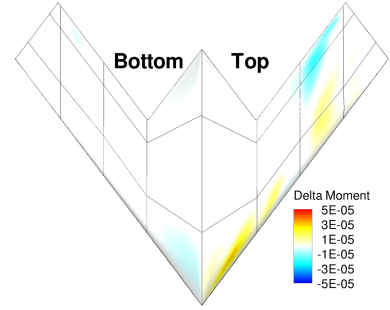
(c) Difference between $\alpha = 10^\circ$ and 14°



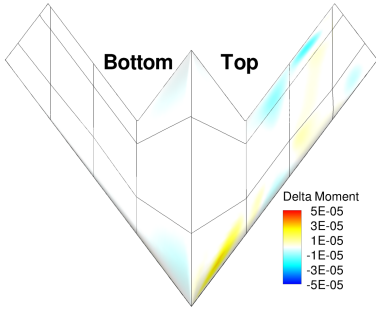
(d) Difference between $\alpha = 14^\circ$ and 15°



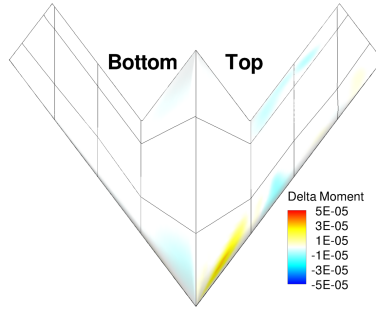
(e) Difference between $\alpha = 15^\circ$ and 16°



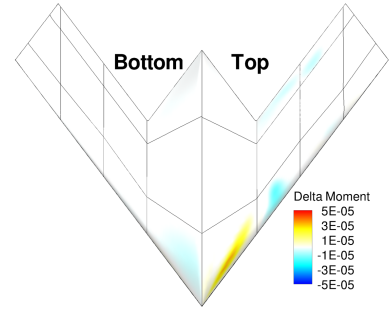
(f) Difference between $\alpha = 16^\circ$ and 17°



(g) Difference between $\alpha = 17^\circ$ and 18°



(h) Difference between $\alpha = 18^\circ$ and 19°



(i) Difference between $\alpha = 19^\circ$ and 20°

Figure 17. Distributions of 'Delta Moment' over the top and bottom SACCON RLE surfaces.

<i>Grid</i>	<i>Characteristic edge dimension N on finest multi-grid level</i>	<i>Number of grid cells</i>
Standard	80	9.088.00
Medium	96	15.704.604
Fine	112	24.937.472

Table 1. Details of the grids used in the grid refinement study.

iterations were employed to ensure a fully converged solution.

The grid converged (asymptotic) value $uh \rightarrow 0$ was computed using formula $uh - uh \rightarrow 0 = Ch\alpha$, where α is the order of the method, h equals the characteristic cell size ($= 1/N$), C is the order constant. The difference between the actual value and the grid converged (asymptotic) value of the lift coefficient, the drag

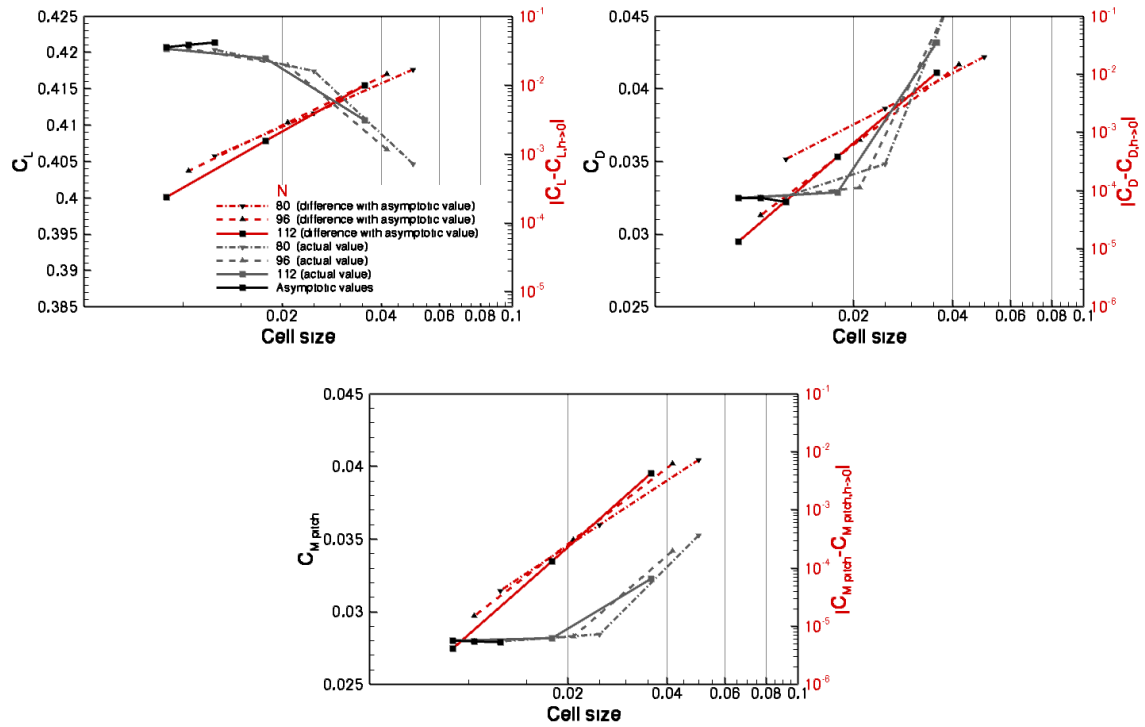


Figure 18. Results of the grid convergence study for the SACCON configuration showing the actual value (gray line), the grid converged (asymptotic) value (black line) and the difference between the actual value and the grid converged (asymptotic) value (red line) as function of the characteristic cell size for the lift coefficient, the drag coefficient and the pitching moment coefficient. The standard grid by the dash-dot line, the medium grid by the dashed line and the fine grid by the solid line.

coefficient and the pitching moment coefficient is shown in Fig. 18. This figure also shows the actual values on each grid level and the grid converged (asymptotic) values. This study showed that as the grid size approaches 25 million grid cells, grid converged solutions are obtained with a difference with respect to the asymptotic value of approximately 10^{-4} for the lift coefficient, approximately 10^{-5} for the drag coefficient and approximately 10^{-5} for the pitching moment coefficient pitch. The drag coefficient shows the largest dependence on the actual grid used. However, on all grids the difference between the actual value and the grid converged (asymptotic) value is for all force and moment coefficients smaller than 10^{-3} , which was considered to be sufficiently small for the present study. Therefore, to save computer costs and moreover to allow the simulation of more cases, the grids for the SLE and RLE model with around 7 million grid points described in Section III have been used.

A comparison is made between the two available CFD codes using the RLE model for a range of angles of attack. This was made based mainly on integral data, which is shown in Fig. 19. The results crossplotted here were obtained from PMB with the $k-\omega$ with vortex correction, to control the production of turbulent kinetic energy, and the baseline $k-\omega$ models and from ENSOLV using the $k-\omega$ model. The lift coefficient plot in Fig. 19 (a) shows a good agreement between the codes in the linear region, all offset from the experiments due to the absence of a sting. The three methods used show a scatter beyond 15° incidence. The break in linearity occurs earliest for the baseline $k-\omega$ at the same incidence where the tip vortex is seen to jump to an inboard position. The $k-\omega$ models stay in good agreement up to 17° incidence which suggests there is turbulence model dependence in the flow solution. A more obvious scatter between computational methods is present in the pitching moment coefficient plot shown in Fig. 19 (b). Both the PMB baseline and ENSOLV $k-\omega$ predict a strong dip although the first does it at 16° incidence and the second at 19° which disagrees with the experiment, at 17.5° . Fig. 20 shows the difference in pressure coefficient distribution over the SACCON predicted with PMB baseline $k-\omega$ and ENSOLV $k-\omega$. An early inboard travel of the onset of the tip vortex is seen in the PMB results, at 16° incidence. Whereas in the ENSOLV solution this does not happen until

the model reaches 19° of incidence. It is clear that in the ENSOLV predictions the dual vortical structure remains up to a higher incidence.

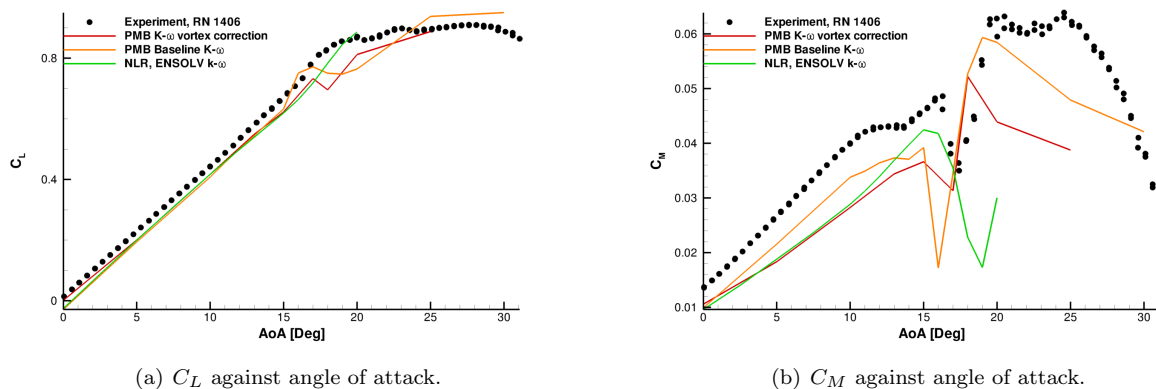


Figure 19. Integral data from experimental results and PMB computations for the round model.

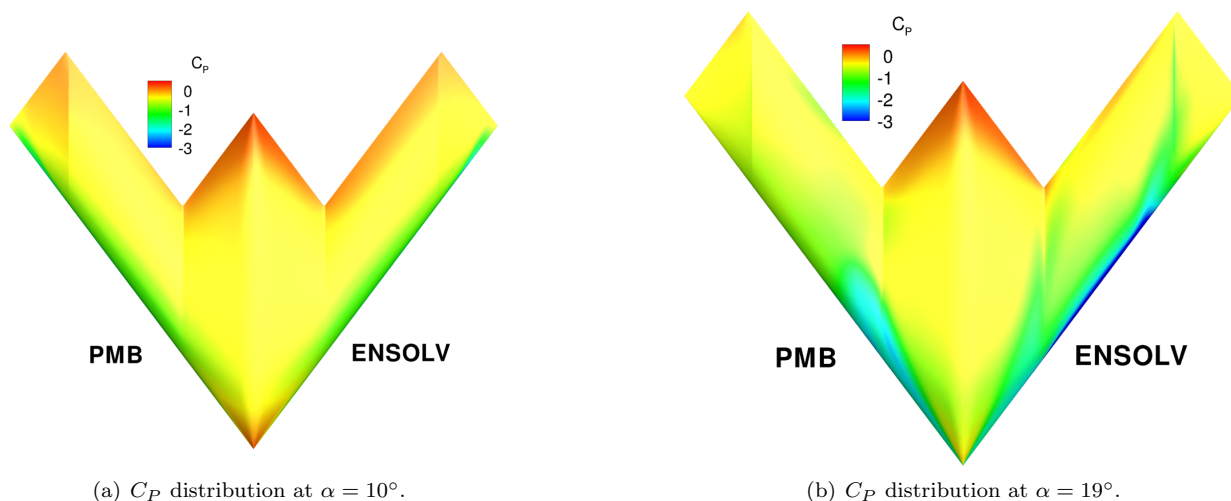


Figure 20. Difference in C_P distribution from Liverpool and NLR solutions.

The experiments show there is some unsteadiness in the flow from 16° angle of attack onwards. Proof of this is the offset in the C_M results from the first to the second run, shown by two black circles at the same incidence in Fig. 19 (b). This repeatability issue could be linked to vortex wandering and oscillation in the position of vortex breakdown which can play a big role in the pitching moment coefficient behaviour. Therefore it is not surprising that the steady RANS methods fail in this region. Based on the integral RLE results it is not obvious which method is most realistic.

V. Results for Forced Oscillatory Motion

Investigations of the aerodynamic characteristics of the SACCON configuration undergoing forced oscillatory motion in pitch axis were examined for the SLE and RLE wind tunnel models.⁷ The paper presents the results of the RLE model at nominal wind tunnel flow conditions. First, the comparison of the integrated aerodynamic coefficients loops is given. Then, the computed surface pressure coefficient distribution at several chordwise locations is shown against measured quantities.

A. Comparison with Wind Tunnel Measurements

Four flow conditions were selected for the RLE wind tunnel model. All cases were run at the same freestream speed and frequency of the applied oscillatory pitching motion. The same moderately small amplitude was also considered. The mean angle of attack was different in all cases, varying from 5.0° up to 20.0° . The nominal flow conditions are summarised in Table 2. Due to experimental uncertainties, it was observed that the flow conditions for which numerical results were computed did not match exactly the conditions of the wind tunnel measurements and, in particular, the instantaneous angle of incidence was lower in the computations than the measurements for the comparisons shown herein.

	Test Case 1	Test Case 2	Test Case 3	Test Case 4
Freestream speed, U_∞	50m/s	50m/s	50m/s	50m/s
Mean incidence, α_0	5.0°	10.0°	15.0°	20.0°
Pitch amplitude, α_a	5.0°	5.0°	5.0°	5.0°
Frequency, f	1Hz	1Hz	1Hz	1Hz

Table 2. Description of RLE wind tunnel model test cases for forced oscillatory motion in pitch axis.

The PMB calculations used the standard $k-\omega$ turbulence model with vortex correction. The pitch motion was simulated for three harmonic periods. The selected numerical parameters, as shown in Table 3, allowed the flow solution to reach a steady harmonic output for all test cases. The non-dimensional time is based on wing mean aerodynamic chord and freestream speed. The reference point for the moments is coincident with the point used in the static investigations. The rotation axis is located further downstream, at 0.8063% of the root chord.

Time steps per cycle	200
Number of cycles	3
Non-dimensional time step, dt	0.5219
Inner iterations per real time step	200

Table 3. Numerical parameters for the RLE wind tunnel model test cases for forced oscillatory motion.

1. Integrated Aerodynamic Coefficients

Forced motion experiments included five repetitive runs in "wind-off" conditions followed by five repetitive runs in "wind-on" conditions. Each "wind-off" run was processed with the corresponding "wind-on" run to eliminate the contributions from mass and inertia forces. For the comparisons to follow, experimental results are included for one representative run only.

The lift and pitching moment coefficient loops for all test cases are compared to experimental measurements. The numerical results contain the time-histories of three oscillatory motions. Transients are damped out rapidly and solutions were well converged. Comparisons for Test Case 1 and 2 are shown in Fig. 21. Next, Fig. 22 shows the results for Test Case 3 and 4. To gain a deeper insight into the forced motion results computed by the PMB solver, static values of aerodynamic coefficients are also included for the same turbulence model used in the present unsteady calculations.

In Fig. 21, the hysteresis in the lift coefficient loops is noticeably small and, in particular, the time-histories compare favourably with the static values. This indicates that the flowfield adapts instantaneously to changes in model attitude and the phase lag of the aerodynamic response to the motion input is reduced to nearly zero. Both static and dynamic results show an offset from experimental measurements. The offset, as mentioned previously, is due to the sting interference, which is not modelled in the PMB computational grid. For the moment coefficient, the forced motion loops differ from the static values. In addition, for Test Case 2 the mean value of the moment coefficient at the mean angle of attack is larger than the static value. The mean slope of the moment loops are steeper than the static slope. The change in static slope observed

beyond 12° is similar to the change in the moment loop for Test Case 2. However, numerical results do not predict the plateau in moment coefficient during part of the cycle.

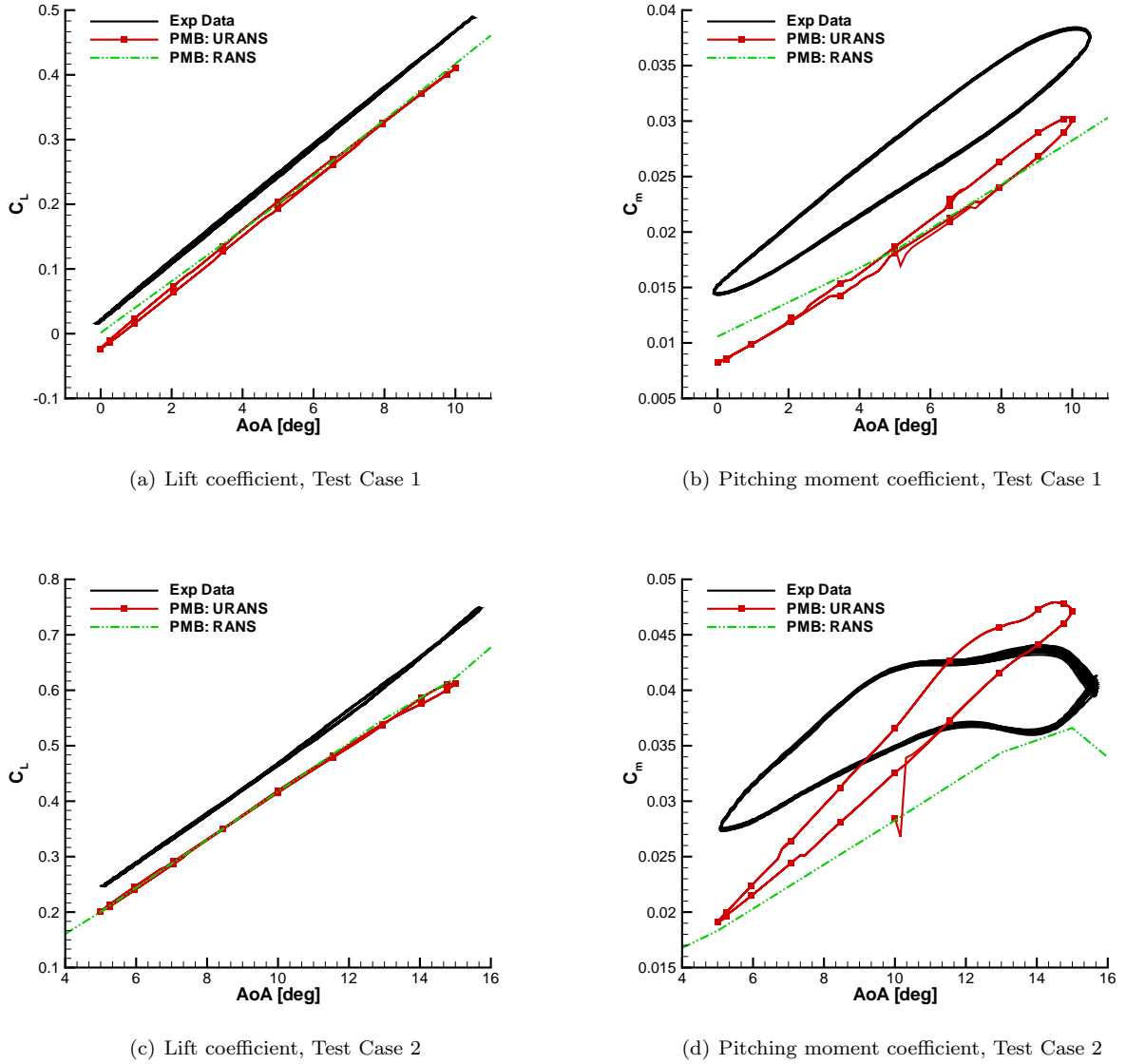
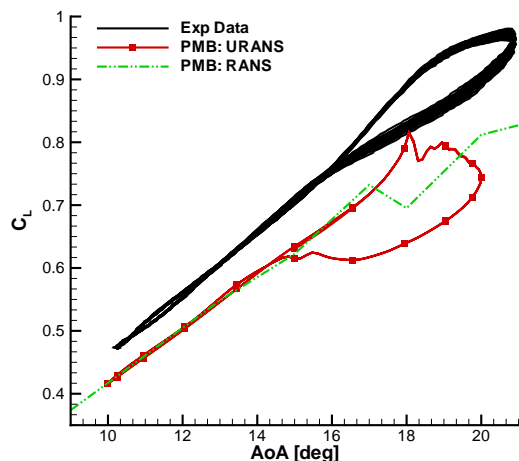


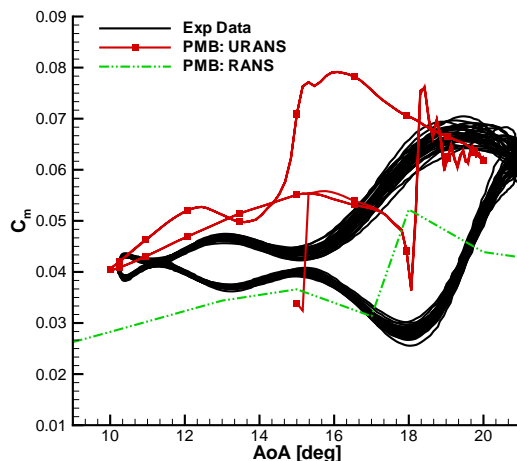
Figure 21. Lift and pitching moment coefficient loops for RLE wind tunnel model for Test Case 1 ($\alpha_0 = 5^\circ$, $\alpha_A = 5^\circ$ and $f = 1Hz$) and Test Case 2 ($\alpha_0 = 10^\circ$, $\alpha_A = 5^\circ$ and $f = 1Hz$).

The comparison for Test Case 3 and 4 is shown in Fig. 22. Flow conditions, which feature harmonically moving vortical flows as the model undergoes the oscillatory motion, impact the shape of the aerodynamic loops. For the force coefficient, the hysteresis is remarkably large at the highest instantaneous angles. Numerical results predict well the main features of the measured lift coefficient loops. Below 15° , the upstroke and downstroke curves are nearly identical for Test Case 3. The same characteristic is found for Test Case 4 below 16° . Beyond these values, numerical solutions compare favourably to experimental data. The reason for measured scatter in the moment coefficient may be related to the flow natural unsteadiness at these angles of incidence. Numerical solutions, which include three oscillatory periods, show a good periodicity. Changes in the mean slope follow similar changes in the static slope and in the experimental results. The plateaux of moment coefficient in the lower and upper part of the loops for Test Case 3 and 4, respectively, show a good agreement with experimental data. However, the solutions fail to predict smooth changes in moment coefficient from 17° up to 19° . Substantial oscillations, which follow a sudden variation

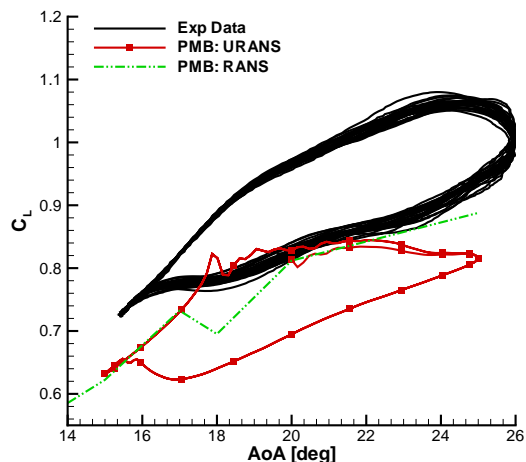
in moment coefficient at exactly the same instantaneous angle of incidence of 18° , damp out during the upstroke motion within the next 2° increment.



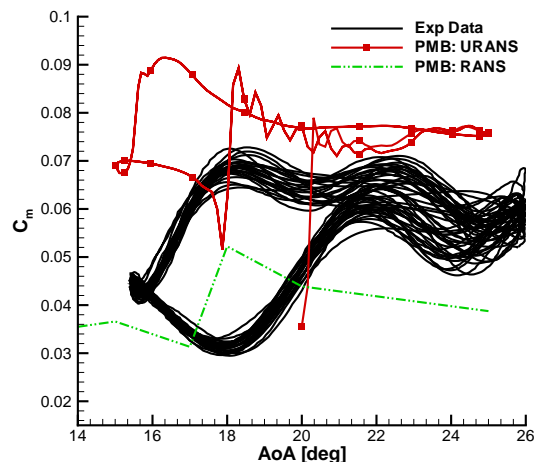
(a) Lift coefficient, Test Case 3



(b) Pitching moment coefficient, Test Case 3



(c) Lift coefficient, Test Case 4



(d) Pitching moment coefficient, Test Case 4

Figure 22. Lift and pitching moment coefficient loops for RLE wind tunnel model for Test Case 3 ($\alpha_0 = 15^\circ$, $\alpha_A = 5^\circ$ and $f = 1Hz$) and Test Case 4 ($\alpha_0 = 20^\circ$, $\alpha_A = 5^\circ$ and $f = 1Hz$).

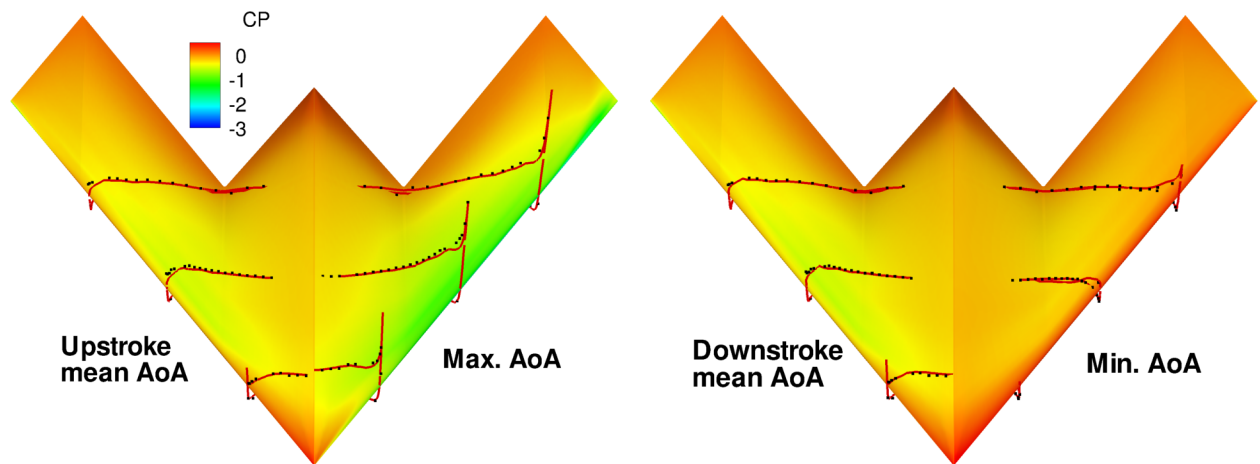
2. Surface Pressure Distribution

For all test cases, the surface pressure coefficient distribution was compared against experimental measurements at three pressure tap sections. Sections RC 20, RC 45 and RC 70 are located at 20%, 45% and 70%, respectively, of the root chord. Data is presented in Figs. 23- 26. Comparison is made at four representative points within one cycle, which feature the flow conditions at the mean angle of attack during upstroke and downstroke motions and at the maximum and minimum angles. The pressure coefficient distributions are plotted versus the fractional distance along the local chord, positive outward.

For Test Case 1, the qualitative agreement of the pressure distribution is good for all stations and all angles of attack. The solution during the upstroke motion is noticeably similar to that at the downstroke motion, strengthening the previous considerations on the instantaneous response of the flow to the input motion. A favourable comparison is also observed in the high suction region near the leading edge. Results

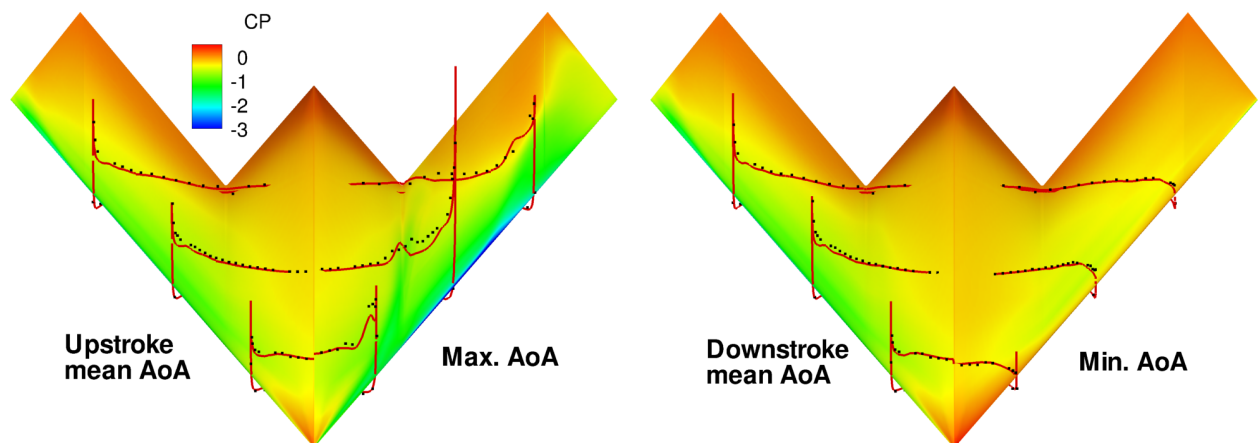
shown to the left in Fig. 24(a) depict the pressure coefficient distributions at the mean angle of attack during the upstroke motion for Test Case 2. Comparison with the results to the right of Fig. 23(a), which represent the solutions at the maximum instantaneous angle for Test Case 1, reveal nearly the same pattern. The pressure distributions at 15° exhibit the development of the inboard and outboard vortices. The strength of the vortices is lower in the simulations than in the experiments and, moving further downstream, the trajectory of the inboard vortex is predicted slightly more inboard. Nearly the same features between upstroke and downstroke motions are obtained from numerical and measured quantities.

Fig. 25 shows the results for Test Case 3, including a complex development of multiple vortices and their moving breakdown point. The strength of the inboard and outboard vortices is generally lower for the simulations. A poor agreement is observed for the most downstream extension of the inboard vortex. At the maximum angle of attack, pressure measurements detect the vortex core to extend up to Section RC 45, and further downstream, the low pressure region is stretched over a larger spanwise section. The vortex breakdown point is predicted far upstream, between Section RC 20 and RC 45. At the downstroke, wiggles are predicted at the most downstream station whereas the measurements show a stronger outboard vortex. As the mean angle of attack is increased for Test Case 4, the location of the vortex breakdown moves upstream toward the leading edge. The strength of the inboard vortex is underpredicted in the simulations at all instants.



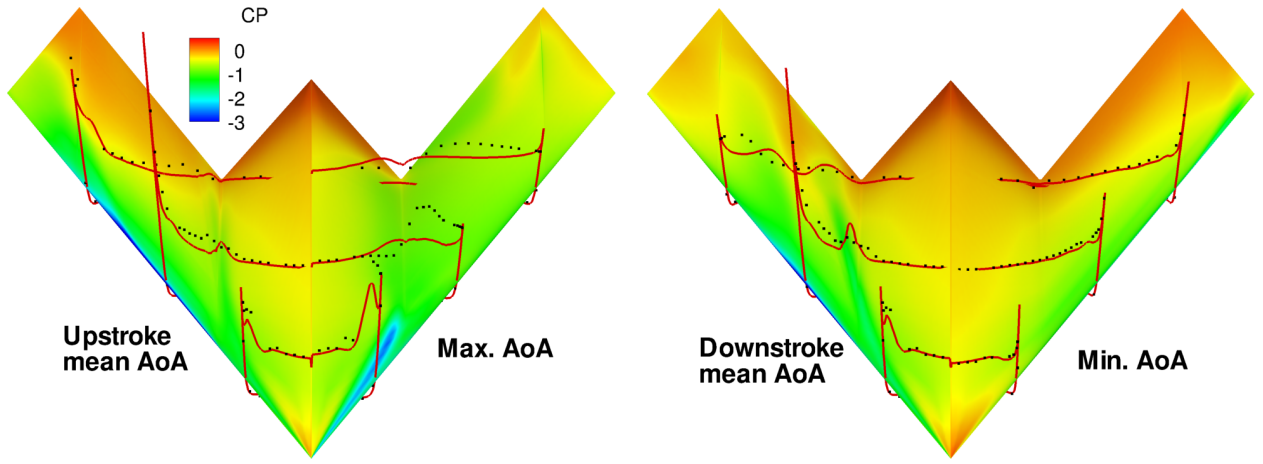
(a) Upstroke ($\alpha = 5^\circ$) and maximum incidence ($\alpha = 10^\circ$). (b) Downstroke ($\alpha = 5^\circ$) and minimum incidence ($\alpha = 0^\circ$).

Figure 23. Surface C_P data across the RLE model for Test Case 1 ($\alpha_0 = 5^\circ$, $\alpha_A = 5^\circ$ and $f = 1Hz$).



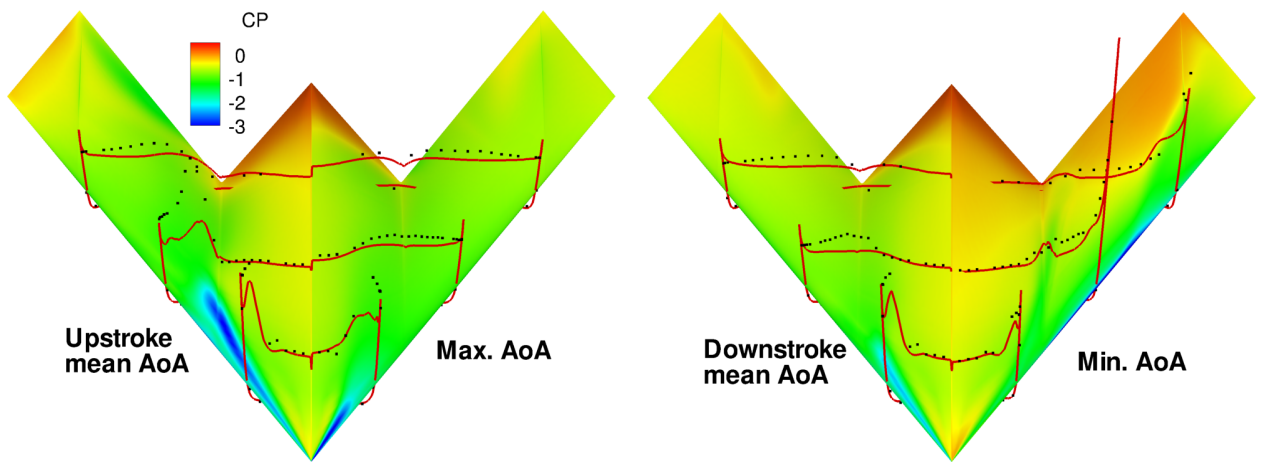
(a) Upstroke ($\alpha = 10^\circ$) and maximum incidence ($\alpha = 15^\circ$). (b) Downstroke ($\alpha = 10^\circ$) and minimum incidence ($\alpha = 5^\circ$).

Figure 24. Surface C_P data across the RLE model for Test Case 2 ($\alpha_0 = 10^\circ$, $\alpha_A = 5^\circ$ and $f = 1Hz$).



(a) Upstroke ($\alpha = 15^\circ$) and maximum incidence ($\alpha = 20^\circ$). (b) Downstroke ($\alpha = 15^\circ$) and minimum incidence ($\alpha = 10^\circ$).

Figure 25. Surface C_p data across the RLE model for Test Case 3 ($\alpha_0 = 15^\circ$, $\alpha_A = 5^\circ$ and $f = 1Hz$).



(a) Upstroke ($\alpha = 20^\circ$) and maximum incidence ($\alpha = 25^\circ$). (b) Downstroke ($\alpha = 20^\circ$) and minimum incidence ($\alpha = 15^\circ$).

Figure 26. Surface C_p data across the RLE model for Test Case 4 ($\alpha_0 = 20^\circ$, $\alpha_A = 5^\circ$ and $f = 1Hz$).

VI. Conclusion

The flow around the SACCON UCAV geometries is highly nonlinear for a range of angles of attack. This is due to the coexistence of two distinct vortices over the model's top surface not only increasing in strength but changing location. The steady state CFD prediction of the flow topology around the SLE model is in better agreement with the experimental measurements than those for the RLE. It has been seen that the leading edge geometry has an important effect on the behaviour of the flow around the model. Sharp leading edges yield vortices which are easier to simulate because of the large adverse pressure gradients forming behind the sharp leading edge and fix the separation line along this edge. Rounded leading edges tend to gradually build up the adverse pressure gradient further downstream which eventually causes flow separation. Predicting the exact location of this separation line is numerically more challenging than having it fixed, as in the SLE configuration. PIV measurements have shown that a more complex vortical structure is present than that initially predicted by numerical methods. It also reinforced the idea that the cause for

the disagreement in vortex locations is due to inadequate modelling of blunt leading edge separation.

The flow around the dynamic model shows interesting hysteresis in lift and pitching moment coefficients beyond $\alpha_0 = 15^\circ$ and $\alpha_0 = 5^\circ$, respectively. The, generally weaker, vortices predicted by the CFD methods result in noticeable disagreement in both static and dynamic force and moment behaviours compared to the measurements. Although, the latter predictions is thought it could still be improved with a finer timestep.

Acknowledgments

This study is supported by an EPSRC and QinetiQ studentship. Computer time was provided though the UK Applied Aerodynamics Consortium (UKAAC) under EPSRC grant EP/F005954/1.

References

- ¹Loeser, T. and Vicroy, D. and Schuette, A., "SACCON Static Wind Tunnel Tests at DNW- NWB and 14x22 NASA LaRC," *28th AIAA Applied Aerodynamics Conference* AIAA-2010-4393, June 2010.
- ²Gilliot, A., "Static and Dynamic SACCON PIV Tests - Part I: Forward Flowfield," *28th AIAA Applied Aerodynamics Conference*, AIAA-2010-4395, June 2010.
- ³Konrath, R. and Roosenboom, E. and Schroder, A. and Pallek, D. and Otter, D., "Static and Dynamic SACCON PIV Tests - Part II: Aft Flow Field," *28th AIAA Applied Aerodynamics Conference*, AIAA-2010-4396. June 2010.
- ⁴Gursul, I. and Gordnier, R. and Visbal, M. "Unsteady aerodynamics of nonslender delta wings," *Progress in Aerospace Sciences* 41 (2005) 515-557.
- ⁵Anderson, J. D., "Fundamentals of Aerodynamics," *McGraw-Hill International 2nd Edition*, 1991.
- ⁶Taylor, G.S. and Gursul, I. "Buffeting Flows over a Low-Sweep Delta Wing," *AIAA Journal*, Vol.42, No9, September 2004.
- ⁷Gordnier, R. E. and Visbal, M. R. and Gursul, I. and Wang, Z., "Computational and Experimental Investigation of a Nonslender Delta Wing," *AIAA Journal*, Vol. 47, No. 8, August 2009.
- ⁸Vicroy, D. and Loeser, T., "SACCON Dynamic Wind Tunnel Tests at DNW- NWB and 14x22 NASA LaRC," *28th AIAA Applied Aerodynamics Conference*, AIAA-2010-4394. June 2010.
- ⁹Badcock, K. J., Richards, B. E. and Woodgate, M. A., "Elements of computational fluid dynamics on block structured grids using implicit solvers," *Progress in Aerospace Sciences* 36, (2000) 351-392.
- ¹⁰Wilcox, D. C., "Turbulence Modelling for CFD," DCW Industries Inc., 3rd Edition, La Cañada, CA, 2006.
- ¹¹Miau, J. J. and Kuo, K. T. and Liu, W. H. and Hsieh, S. J. and Chou, J. H., "Flow Developments Above 50-Deg Sweep Delta Wings with Different Leading-Edge Profiles," *Journal of Aircraft*, Vol. 34, No. 4, July-August 1995.
- ¹²Boerstoel, J.W., Kassies, A., Kok, J.C., and Spekrijse. S.P., "ENFLOW, a Full-Functionality System of CFD Codes for Industrial Euler/Navier-Stokes Flow Computations," NLR TP 96286U, NLR, Amsterdam, 1996
- ¹³Menter, F. R., "Zonal Two Equation $k-\omega$ Turbulence Models for Aerodynamic Flows," *24th AIAA Fluid Dynamics Conference* 93-2906, July 6-9 1993, Orlando, Florida.
- ¹⁴Yaniktepe, B. and Rockwell, D., "Flow Structure on a Delta Wing of Low Sweep Angle," *AIAA Journal* 2004, 42(3): 513-23.
- ¹⁵Schuette, A., "Numerical and Experimental Analyses of the Vortical Flow Around the SACCON Configuration," *28th AIAA Applied Aerodynamics Conference*, AIAA-2010-4690, June 2010.
- ¹⁶Cummings, R., "SACCON Static and Dynamic Motion Flow Physics Simulations Using COBALT," *28th AIAA Applied Aerodynamics Conference*, AIAA-2010-4691, June 2010.
- ¹⁷Le Roy, J., "SACCON CFD Static and Dynamic Derivatives Using elsA," *28th AIAA Applied Aerodynamics Conference*, AIAA-2010-4562, June 2010.
- ¹⁸Gilliot, A., "Static and Dynamic SACCON PIV Tests - Part I: Forward Flowfield," *28th AIAA Applied Aerodynamics Conference*, AIAA-2010-4395, June 2010.
- ¹⁹Konrath, R., Roosenboom, E., Schrder, A., Pallek, D. and Otter, D., "Static and Dynamic SACCON PIV Tests - Part II: Aft Flow Field," *28th AIAA Applied Aerodynamics Conference*, AIAA-2010-4396, June 2010.